

Simple harmonic oscillator based reconstruction and estimation for one-dimensional q -space magnetic resonance (1D-SHORE)

Evren Özarslan, Cheng Guan Koay, and Peter J. Basser

Abstract The movements of endogenous molecules during the magnetic resonance acquisition influence the resulting signal. By exploiting the sensitivity of diffusion on the signal, q -space MR has the ability to transform a set of diffusion-attenuated signal values into a probability density function or propagator that characterizes the diffusion process. Accurate estimation of the signal values and reconstruction of the propagator demand sophisticated tools that are well-suited to these estimation and reconstruction problems. In this work, a series representation of one-dimensional q -space signals is presented in terms of a complete set of orthogonal Hermite functions. The basis possesses many interesting properties relevant to q -space MR, such as the ability to represent both the signal and its Fourier transform. Unlike the previously employed cumulant expansion, biexponential fit and similar methods, this approach is linear and capable of reproducing complicated signal profiles, e.g., those exhibiting diffraction peaks. The estimation of the coefficients is fast and accurate while the representation lends itself to a direct reconstruction of ensemble average propagators as well as calculation of useful descriptors of it, such as the return-to-origin probability and its moments. In axially symmetric and isotropic geometries, respectively, two- and three-dimensional propagators can be reconstructed from one-dimensional q -space data. Useful relationships between the one- and higher-dimensional propagators in such environments are derived.

Evren Özarslan

Section on Tissue Biophysics and Biomimetics (STBB), PPITS, NICHD, NIH and Center for Neuroscience and Regenerative Medicine, USUHS. e-mail: evren@helix.nih.gov

Cheng Guan Koay

Department of Medical Physics, University of Wisconsin, Madison. e-mail: cgkoay@wisc.edu

Peter J. Basser

Section on Tissue Biophysics and Biomimetics (STBB), PPITS, NICHD, NIH. e-mail: pjbasser@helix.nih.gov

1 Introduction

Diffusion is a transport process characterized by the spontaneous and incessant movements of particles. The characteristics of the diffusion process are determined by the structure of the host matrix. As such, one can obtain information about the domain in which diffusion is taking place by observing diffusion. One widespread method for measuring diffusion involves the nuclear magnetic resonance (NMR or MR) technique whose sensitivity to diffusion of spin-bearing molecules was realized in its earliest days [9]. Later on, it was demonstrated that by incorporating a pair of pulsed magnetic field gradients into conventional MR acquisitions, one can observe diffusion in a convenient and controllable way [38]. This “pulsed-field-gradient” (PFG) MR technique enabled the examination of numerous substances in diverse areas. A spin that is moving between the application of the two diffusion sensitization pulses of the PFG experiment suffers a net phase shift. A population of randomly moving spins yield an incoherent phase profile, which leads to an attenuation of the MR signal [17].

In diffusion MR, the net displacement vector \mathbf{R} is a Fourier-conjugate to an experimentally controlled variable $\mathbf{q} = \gamma\delta\mathbf{G}/(2\pi)$, where γ is the gyromagnetic ratio, δ is the duration of the diffusion gradient pulses and \mathbf{G} is the diffusion gradient vector, i.e. [37, 13],

$$P_{3D}(\mathbf{R}) = \int d\mathbf{q} e^{i2\pi\mathbf{q}\cdot\mathbf{R}} E(\mathbf{q}). \quad (1)$$

Here, $E(\mathbf{q})$ is the MR signal attenuation and, when δ is small, $P_{3D}(\mathbf{R})$ is an ensemble average propagator indicating the probability for molecules to undergo a displacement \mathbf{R} in the interval between the two pulses. Therefore, $P_{3D}(\mathbf{R})$ can be estimated from data obtained via sampling the three-dimensional “ q -space” and then employing a Fourier transform scheme.

Frequently, because of experimental limitations or because the desired characteristics of the specimen can be extracted from one-dimensional data, the entire three-dimensional q -space is not sampled. Instead, a one-dimensional version of the q -space acquisition is performed by keeping the direction of the diffusion gradients fixed, and varying only their strength. If the x -axis is defined to be the direction of the gradients, then a one-dimensional average propagator can be obtained from the relationship

$$P(x) = \int dq e^{i2\pi qx} E(q). \quad (2)$$

By sensitizing the signal to the random motion of the molecules, the q -space MR technique enables the study of microscopic compartments whose dimensions cannot be resolved by conventional MR imaging and microscopy. Moreover, the one-dimensional average propagator was shown to provide information about diffusion, flow, restrictions to motion and even spatially dependent relaxation sinks [6]. In one application of diffusion acquisitions involving specimens with an ordered microstructure, the non-monotonic dependence of the q -space signal on q [4, 23] was exploited to determine cell sizes. In another application, the q -space signal has been

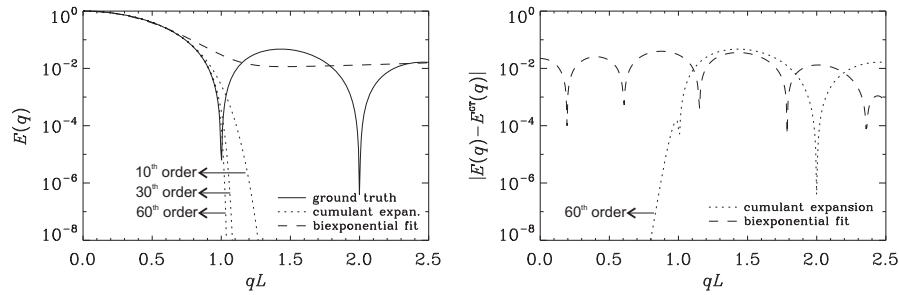


Fig. 1 MR signal attenuation expected from spins diffusing inside a rectangular pore of length L is depicted via the continuous line on the left panel. Also shown on this panel are the curves obtained from a biexponential fit (dashed line) and cumulant expansion with 10th, 30th and 60th order approximations (dotted lines). The right panel shows the errors acquired in the biexponential fit and the 60th order cumulant expansion. In these simulations, the biexponential fit was obtained from 400 points uniformly covering a qL interval of [0,2.5]. The cumulant expansions are obtained by analytically expanding the logarithm of the signal attenuation in a power series.

used to estimate scaling exponents that were related to the fractal dimension of disordered media [25]. Since the diffusion propagator is a probability density function, among its descriptors are the moments of this density function. Another important quantity is the probability for no net displacement, or more commonly referred to as the return-to-origin probability [10]. These quantities are all indicators of tissue microstructure, which could be altered by changes due to development, aging, and disease.

Estimation of the derived quantities and reconstruction of the propagators can be significantly improved if the signal decay can be expressed parametrically. For this purpose, biexponential fitting [5, 31] and cumulant expansion [39, 18, 16, 11] techniques have been applied to q -space data. However, both of these approaches are limited in their ability of reproducing general $E(q)$ profiles. For example, biexponential functions are monotonic by design, and as such, they can not possibly model non-monotonic diffraction-like features. The cumulant expansion method is bound to fail as well, because the signal minima are typically at or beyond the radius of convergence [7, 14] for such expansions. Moreover, Pawula's theorem guarantees that the propagators reconstructed from a cumulant expansion terminated beyond the Gaussian term will have unacceptable properties [32]. Figure 1 illustrates how both of these methods fail in reproducing the exact MR signal attenuation from spins diffusing inside a rectangular pore. Other parameterizations of the q -space signal include the assignment of a continuous spectrum of diffusivities [33, 36, 42] and fitting stretched exponential [15, 2] or Rigaut-type asymptotic fractal expressions [15, 12] to diffusion-attenuated MR data. These parametric representations also suffer from the above-mentioned problems.

In this work, we propose expressing the one-dimensional q -space MR signal in terms of the eigenfunctions of the quantum-mechanical simple harmonic oscillator Hamiltonian, sometimes called the Hermite functions, which form a complete or-

thogonal basis for the space of square integrable functions [21]. Because Fourier transforms of these functions are Hermite functions themselves, our approach directly yields a propagator expressed in the same set of basis functions. Estimation of probability distributions in a series of Hermite functions is well-studied in the statistics literature [35] and such expansions were shown to possess powerful properties, such as rapid convergence in both real and Fourier spaces [41], which suit problems of q -space signal analysis and average propagator estimation.

After introducing the basis and a numerical estimation method for its coefficients in the next section, in Section 3, we evaluate the accuracy of the signal, propagator, moment and return-to-origin probability estimates. Several important and useful relationships regarding the employed basis and geometries with axial symmetry or isotropic environments are derived in the appendices.

2 Theory

We propose to express the diffusion-weighted MR signal as

$$S(q) = \sum_{n=0}^{N-1} a'_n \phi_n(u, q), \quad (3)$$

with

$$\phi_n(u, q) = \frac{i^{-n}}{\sqrt{2^n n!}} e^{-2\pi^2 q^2 u^2} H_n(2\pi u q). \quad (4)$$

Here $H_n(x)$ is the n th order Hermite polynomial and u is a characteristic length to be determined. The MR signal attenuation, defined to be $E(q) = S(q)/S(0)$, can be expressed in the same basis as

$$E(q) = \sum_{n=0}^{N-1} a_n \phi_n(u, q), \quad (5)$$

where

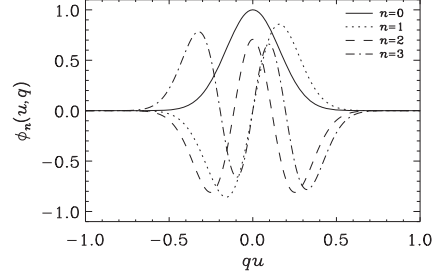
$$a_n = \frac{a'_n}{S_0}, \quad (6)$$

with $S_0 = S(0)$ is the signal with no diffusion weighting, which can be estimated from the coefficients a'_n :

$$S_0 = \sum_{n=0}^{N-1} a'_n \phi_n(u, 0) = \sum_{n=0,2,4,\dots}^{N-1} \frac{(n-1)!!}{\sqrt{n!}} a'_n. \quad (7)$$

Note that the ϕ_n functions are related to the eigenfunctions of the quantum-mechanical simple harmonic oscillator Hamiltonian. It is well-known that these functions form a complete orthogonal basis for the space of square-integrable functions [21]. Figure 2 depicts first few of these functions. One important property of

Fig. 2 First four functions used in the expansion of the MR signal profiles, $S(q)$. Note that the real and imaginary parts of, respectively, the even- and odd-order functions are plotted as the other parts are 0.



these functions is that their Fourier transforms are also Hermite functions; this enables direct estimation of the propagator through the expression

$$P(x) = \sum_{n=0}^{N-1} a_n \psi_n(u, x), \quad (8)$$

where

$$\begin{aligned} \psi_n(u, x) &= \frac{i^n}{\sqrt{2\pi u}} \phi_n\left(\frac{1}{2\pi u}, x\right) \\ &= \frac{1}{\sqrt{2^{n+1} \pi n! u}} e^{-x^2/(2u^2)} H_n(x/u). \end{aligned} \quad (9)$$

Note that the functions $\psi_n(u, x)$ are real-valued, which assures that the probabilities will be real-valued when the a_n are real. This is a consequence of the phase convention we have employed in Eq. 4, which ensures that the real and imaginary parts of the signal are even and odd, respectively. Moreover, Eq. 6 guarantees that the total probability, i.e., the integral of the function $P(x)$, will be unity. See Appendix 1 for some additional properties of this basis.

2.1 Implementation

A set of a'_n coefficients can be estimated by solving a set of linear equations. To see this, we shall denote by \mathbf{S} the M -dimensional vector of signal values. The m th component of this vector is $S_m = S(q_m)$. Similarly, an $M \times N$ dimensional matrix, \mathbf{Q} , can be defined with components $Q_{mn} = \phi_n(u, q_m)$. The estimation problem is reduced simply to a matrix equation $\mathbf{S} = \mathbf{Q}\mathbf{a}'$, where the N -dimensional vector of a'_n coefficients is denoted as \mathbf{a}' . In our implementation, this equation was solved by computing the pseudoinverse of \mathbf{Q} via singular value decomposition [34]. S_0 is computed subsequently using Eq. 7, which is inserted into Eq. 6 to determine the coefficients a_n .

It is important to note that a prior estimate of u is necessary for the above estimation scheme. An adequate choice of u is necessary to obtain a reasonable approximation of the signal with few terms in the series. To this end, in our implementation, we first estimated a maximum value for u from the first few points of $S(q)$; in this range of q -values, the signal was assumed to undergo Gaussian attenuation. Note that when the signal is Gaussian, all coefficients except a_0 vanish, and the signal attenuation is given by $E(q) = \exp(-2\pi^2 q^2 u^2)$. Starting with this estimate of u , we gradually reduced it and at each value of u , we estimated the a_n coefficients using the above scheme. Next, the signal attenuation values at the data points corresponding to the particular u and a_n values were computed. These values shall be denoted by $E^{\text{est}}(u, q)$. The mean error defined by

$$\varepsilon(u) = \frac{1}{M} \sum_{i=1}^M (E^{\text{est}}(u, q_i) - E^{\text{data}}(q_i))^2, \quad (10)$$

was evaluated at each step, where $E^{\text{data}}(q_i)$ are the original data points. The search for the optimal u was discontinued when a local minimum is achieved, or $\varepsilon(u)$ fell below 1×10^{-15} . The last set of u and a_n values were used in subsequent analysis.

The average probability estimates can be computed for arbitrary values of x using Eqs. 8-9. A return-to- yz -plane probability can be estimated either from the $x = 0$ point of $P(x)$, or directly from Eqs. 26 with 22. The moments, $\langle x^m \rangle$, can be computed from the coefficients a_n using Eq. 25.

Many examples of media of interest to the MR community exhibit certain levels of symmetry such as full isotropy or axial symmetry. For such specimens, one-dimensional $E(q)$ data is sufficient to reconstruct two- and three-dimensional average propagators in cases of axial symmetry and isotropy, respectively. It was shown that such higher-dimensional propagators may be more meaningful than the one-dimensional propagator [27]. For the case of axial symmetry, several general relationships exist between the one- and two-dimensional propagators and their moments along with the expressions of the same quantities in terms of the a_n coefficients. These are derived in Appendix 3. Finally, Appendix 4 includes the derivations of similar relationships between one- and three-dimensional propagators for isotropic geometries.

3 Results

We test our estimation and reconstruction scheme on six different signal attenuations with analytically (i.e., exactly) available average probability profiles and moments. Table 1 includes the percentage deviations of the zero-displacement probabilities as well as even-order moments, estimated using the proposed series representation, from the exact ground truth values for five of the geometries considered.

From its first days, PFG-MR techniques have been used to measure the bulk diffusion coefficients of fluids. In this case, the signal as well as the average propa-

gator is Gaussian. Similarly, when the sample has two distinct, non-exchanging, but freely diffusing compartments, the signal and the average propagators can be written in terms of sums of two Gaussians. It has been shown in numerous studies that biexponential fits are quite satisfactory in modeling typical signal decays observed from real tissue [20, 19]. Therefore, it is very important for a new reconstruction scheme to fit mono- and bi-exponential decays. Figure 3 illustrates the performance of the approach in mono- and bi-exponential signal attenuations where diffusion coefficient was taken to be $1.0 \times 10^{-3} \text{mm}^2/\text{s}$ in the mono-exponential case. In the simulations of bi-exponential attenuation, the diffusion coefficients were taken to be $1.5 \times 10^{-3} \text{mm}^2/\text{s}$ and $2.5 \times 10^{-4} \text{mm}^2/\text{s}$ with volume fractions of 0.6 and 0.4, respectively. 33 sampling points were used, and a total of 12 even-ordered a_n coefficients were kept in the series representation under the assumption that the propagator is symmetric. The first row depicts the signal attenuation values (left) as well as the deviation of the estimated signals from the ground truth (right). In the case of mono-exponential attenuation, the scheme is exact up to numerical precision while the performance is very accurate for biexponential decay as well. The figure demonstrates that the scheme yields not only a good approximation within the sampling window, but also a satisfactory extrapolation of the decay curve outside the sampling window. The second, third and fourth rows of the figure illustrate the results obtained from the one-, two- and three-dimensional Fourier transforms of the signal decay curves. The two-dimensional Fourier transform was performed under the assumption that the signal originated from an axially symmetric environment, while the three-dimensional Fourier transform assumed isotropy. In these cases, one-dimensional q -space data is sufficient to reconstruct these higher-dimensional propagators as detailed in Appendices 3 and 4. In all cases, the reconstructed propagators are indistinguishable from the ground truth propagators.

To show the performance of the scheme for non-symmetric displacement probabilities, we simulated a flowing fluid with the assumption that the molecules undergo a net coherent displacement of $1.5u$. In the presence of flow, the expected signal attenuation is complex-valued and the odd-ordered coefficients of the series in Eq. 3 have to be retained. Our simulations started with 33 complex data points and N was set to 23. The results shown in Figure 4 indicate that the errors in the signal decay as

Table 1 Percent (%) deviations of the estimated quantities from their exact values.

	monoexponential	biexponential	rectangular pore	cylindrical pore	spherical pore
S_0	3.0×10^{-14}	7.0×10^{-7}	4.2×10^{-12}	4.3×10^{-12}	1.9×10^{-13}
$P(0)$	5.7×10^{-13}	4.0×10^{-2}	3.3	1.7×10^{-1}	1.3×10^{-2}
$P_{2D}(0)$	4.0×10^{-12}	2.2×10^{-1}	—	4.3	—
$P_{3D}(0)$	1.9×10^{-11}	6.9×10^{-1}	—	—	5.7
$\langle x^0 \rangle$	0	4.4×10^{-14}	1.6×10^{-6}	7.4×10^{-7}	5.1×10^{-10}
$\langle x^2 \rangle$	4.1×10^{-13}	4.3×10^{-5}	5.1×10^{-5}	2.4×10^{-5}	1.0×10^{-7}
$\langle x^4 \rangle$	5.0×10^{-12}	5.6×10^{-4}	6.7×10^{-4}	2.9×10^{-4}	2.5×10^{-6}
$\langle x^6 \rangle$	3.4×10^{-11}	3.9×10^{-3}	6.7×10^{-3}	3.0×10^{-3}	3.8×10^{-5}

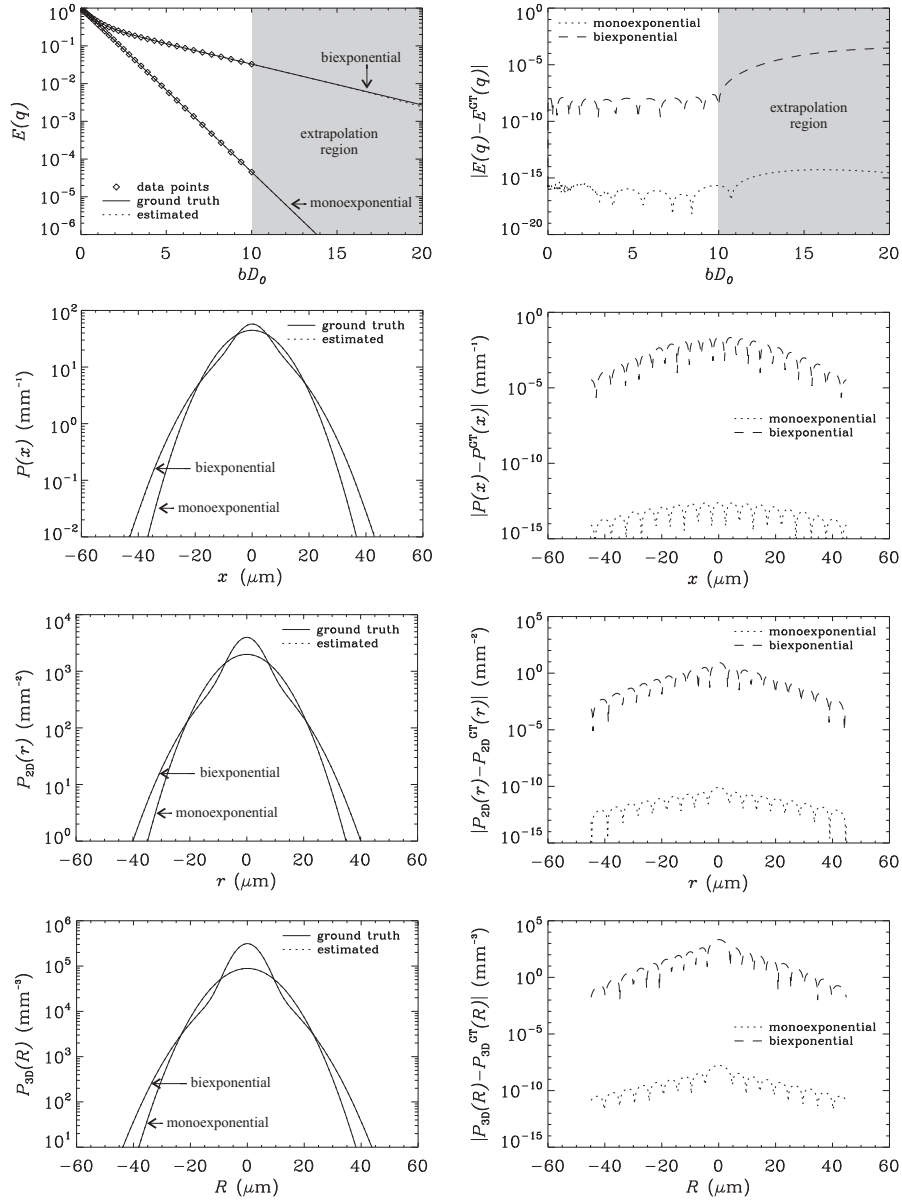


Fig. 3 Signal decay profiles, and one-, two- and three-dimensional propagators (left column, from top to bottom) including both the ground truth and estimated curves from monoexponential as well as biexponential diffusion. The right column shows the associated errors in the estimates. Note that the two- and three-dimensional propagators are symmetrized around the 0 radius to make comparisons with the one-dimensional propagator convenient.

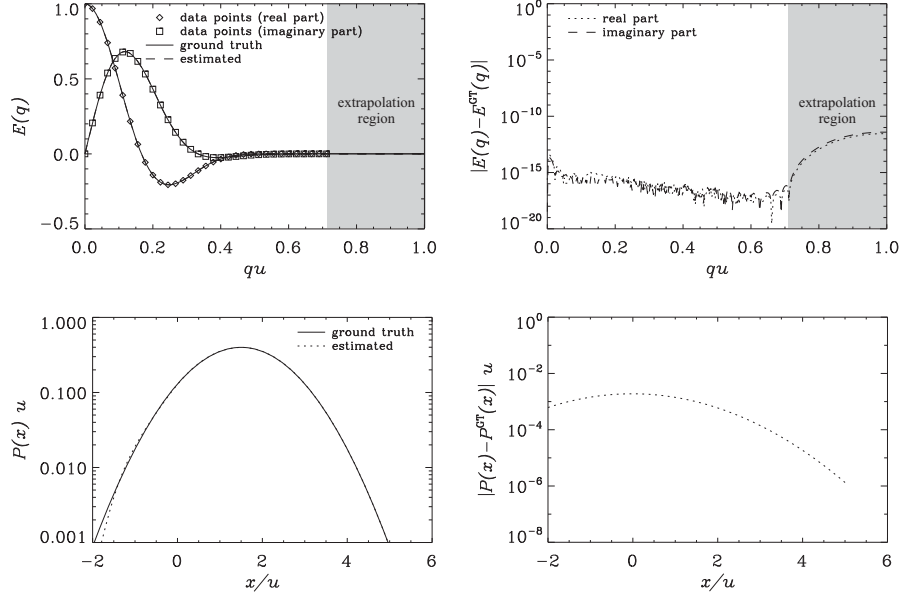


Fig. 4 Diffusion signal decay, and the corresponding average propagator (left column, from top to bottom) from the simulations of Gaussian diffusion with flow. Note that the signal is complex-valued due to flow, which yields a horizontal shift in the reconstructed average propagator. The right column shows the associated errors in the estimates.

well as in the reconstructed average propagator is negligible and the peak of the displacement probability shifted by the correct distance. Note that because of the lack of symmetry, the zero-displacement probabilities are not meaningful for this set of simulations. Additionally, unlike in the other geometries considered, the propagator in the presence of flow has non-zero odd-ordered moments. Consequently, we did not include the percentage deviations from this simulation in Table 1. The percentage deviation of the estimated S_0 from the correct one was only 9.7×10^{-14} . The percent deviations in the moments $\langle x^0 \rangle$ through $\langle x^7 \rangle$ were 4.4×10^{-14} , 9.7×10^{-11} , 3.5×10^{-9} , 2.6×10^{-8} , 3.6×10^{-7} , 1.4×10^{-6} , 1.1×10^{-5} , 3.0×10^{-5} .

Next we tackle three different scenarios of restricted diffusion. All of these simulations start with generating 33 data points and a total of 28 terms in the series of Eq. 3 are kept. First, we simulate the signal attenuation from a one-dimensional geometry in which the molecules are trapped between two parallel plates separated from each other by a distance L . When the diffusion time is long, the diffraction-like features are apparent, which leads to a challenging signal decay profile to estimate. However, as shown in the first row of Figure 5, the proposed basis performs well not only in the sampling window but also in the extrapolation region. Note the tremendous improvement over the results obtained from biexponential fitting as well as cumulant expansion as was illustrated in Figure 1. This improvement was achieved

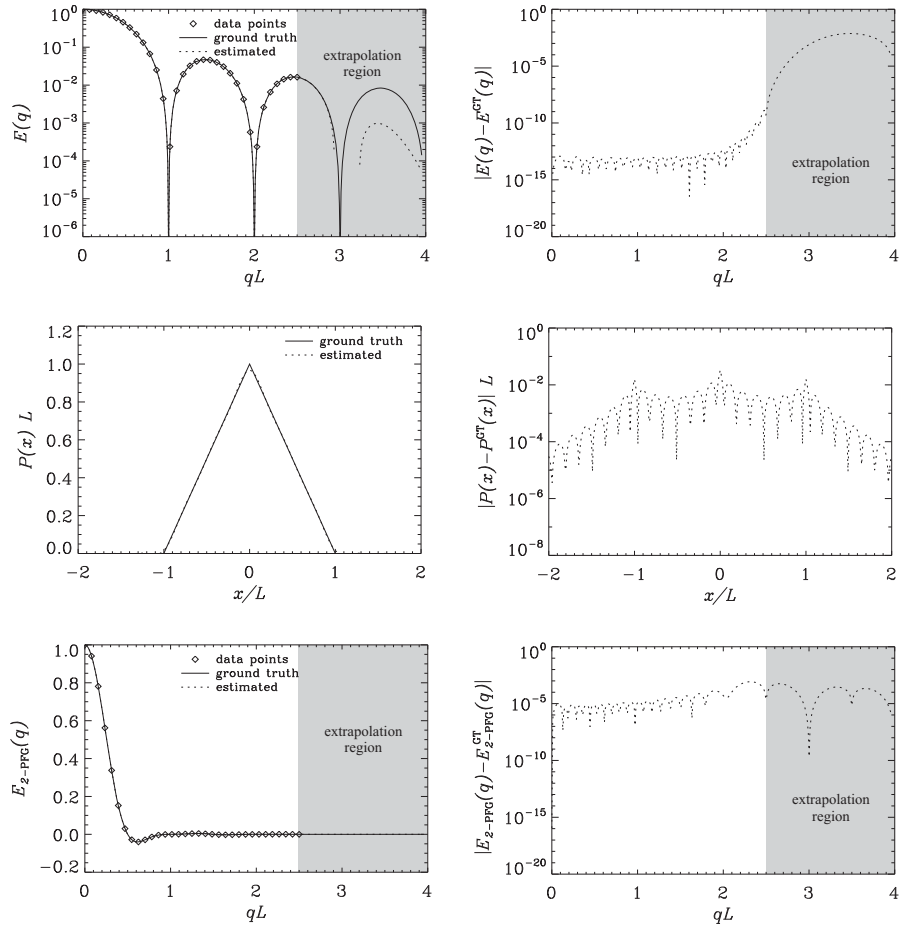


Fig. 5 Signal decay expected from a rectangular pore obtained via a single-PFG experiment and the error in its SHORE estimate (top row). These images are the SHORE counterpart of the cumulant expansion and biexponential fitting results presented in Figure 1. The associated average propagator and the error in the reconstruction is shown in the middle row. The bottom row shows the signal expected from a double-PFG experiment. Note that unlike in the case of the single-PFG experiment, this plot is not logarithmic, which was necessary to accommodate negative portions of the curve.

in spite of the fact that the analytical form of the cumulant expansion was used and the biexponential fitting was performed on 400 data points. In contrast, our SHORE simulation was numerical and used less than 10% of the data points within the same window.

The corresponding propagator is given by a triangular function which is not differentiable at three points. Although our basis is composed of smooth functions, the approximation is quite successful for this piecewise smooth function (see the second

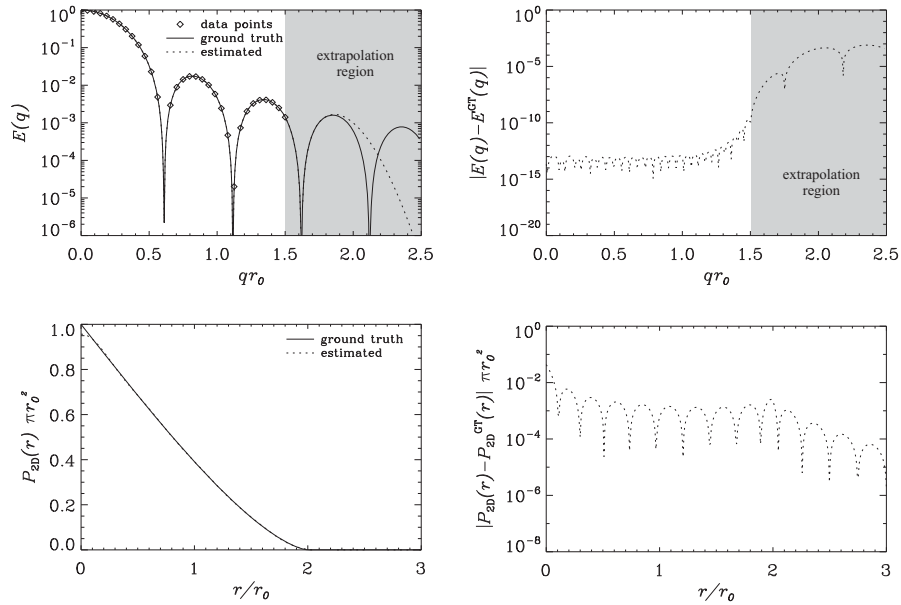


Fig. 6 Signal decay curve, and two-dimensional axially-symmetric propagator (left column, from top to bottom) for the cylindrical pore with radius r_0 . The associated errors are depicted in the right column.

row of Figure 5). Finally, in the last row of the same figure, we consider the diffraction pattern predicted for a double-PFG experiment [23]. In such experiments, rather than bouncing back from the horizontal axis, the signal decay is expected to cross the horizontal axis and become negative at exactly half the q -value of the corresponding single PFG experiment [23]. The satisfactory performance of the approach for this more oscillatory signal attenuation profile suggests that the approximation can be used to model signal decays obtained from multiple PFG sequences.

The second simulated restricted diffusion scenario is diffusion taking place inside a cylinder of radius r_0 . The simulations of this axially symmetric geometry were performed with identical parameters and the two-dimensional axially-symmetric Fourier transform was computed both exactly and also from the a_n coefficients as described in Appendix 3. The results are presented in Figure 6. Finally in Figure 7 we depict the results obtained from simulations of diffusion inside a sphere of radius R_0 . For this geometry both the one- and three-dimensional average propagators are included. Note that the two- and three-dimensional average propagators obtained from the cylindrical and spherical pores resemble the triangular propagator obtained from the rectangular pore. This observation suggests that the true displacement profile is approximately linear in these geometries—a finding that cannot be gleaned by studying the form of one-dimensional propagators.

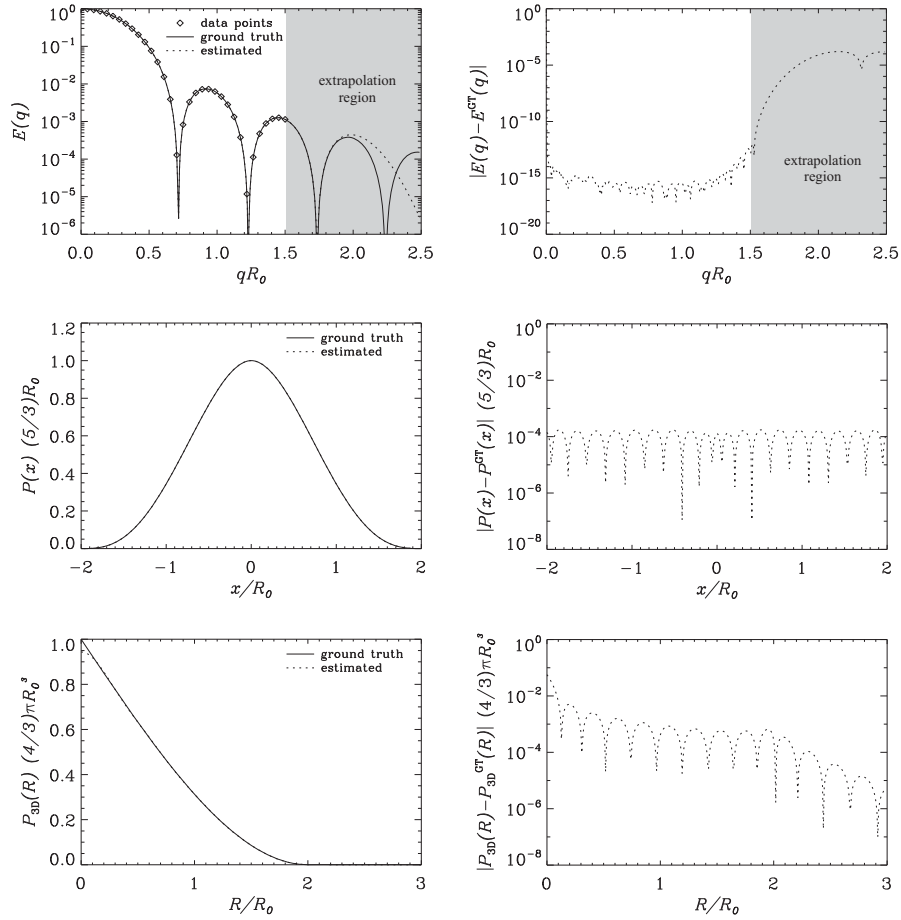


Fig. 7 Signal decay profile, and one-dimensional and three-dimensional isotropic propagator (left column, from top to bottom) for the spherical pore with radius R_0 . The associated errors in the estimates are included in the right column.

The results presented in Table 1 demonstrate the accuracy of the quantities that are computed directly from the a_n coefficients using the relations derived in the appendices. Note that zero-displacement probabilities are typically more difficult to estimate because of their sensitivity to the signal values over the entire q -axis. Therefore, extrapolations become more significant in these estimations. Similarly, the higher order moments are related to the higher order derivatives of the signal decay at the origin. Therefore, the accuracy in the estimates of the moments is an indication of the accuracy in the derivatives of $E(q)$ at $q = 0$. Finally, we would like to note that because the one-dimensional moments are directly proportional to the two- and three-dimensional radial moments, as implied by Eqs. 41 and 56, the

percent deviations in the radial moments are identical to those in one-dimensional moments. Consequently, these deviations are not included in Table 1.

4 Discussion

We would like to point out that the two- and three-dimensional average propagators were not qualitatively different from their one-dimensional counterparts in the simulations of mono- and bi-exponential attenuations. However, in the case of restricted diffusion, e.g., inside a spherical pore, as seen in Figure 7, the propagator obtained from the three-dimensional Fourier transform resembles the one-dimensional triangular propagator for diffusion inside a rectangular pore although the one-dimensional propagator of the spherical pore is smoother and Gaussian-like. This is an indication that the violation of the Gaussian phase approximation is more severe in one-dimensional geometries, because in one-dimensional propagators of higher-dimensional pores, displacements are projected onto one of the axes leading to a smoothing effect in such environments. Moreover, since the propagator is the autocorrelation function of the shape function, it is straightforward to prove that, in closed pores, the zero-displacement probability is just the reciprocal of the pore “volume.” As can be seen in Eqs. 29, 46, and 61, this was exactly the case for the zero-displacement values of the one-, two- and three-dimensional propagators for rectangular, cylindrical and spherical pores, respectively. The $x = 0$ values of the one-dimensional propagators for cylindrical and spherical pores (see Eqs. 47 and 63) suggest that there may not be such a shape-independent relation between the $P(x = 0)$ value of a higher-dimensional geometry and the shape of the pore.

The technique we have presented here is linear because the estimated coefficients, a'_n , are expressible as a linear combination of the signal values. In fact, to estimate the coefficients of the series representation, we posed the problem as a matrix equation. The scheme demands an *a priori* estimate of the characteristic length u . This can be done using many different ways; the approach we have described in the Theory section starts by fitting the small- q section of the $E(q)$ data to a Gaussian decay curve, i.e., $E(q) \approx e^{-2\pi^2 q^2 u^2}$, and gradually reducing the u -value until the mean error, i.e., the average squared deviation of the signal attenuation estimates from the original values, reaches a minimum or drops below a very small value comparable to the machine precision. Note that the estimation of a maximum value for u from the first few points of the signal profile is nonlinear, and because it is performed on fewer data points, the estimates are prone to error. However, the completeness of the employed basis, regardless of u , guarantees the convergence of the series although a deviation in the estimated u -value from its ground-truth value may affect the rate of this convergence. In our simulations, we observed that even 10% error in the estimation of u was tolerable and did not change the quality of the results significantly.

As discussed above, the constant u is a characteristic length proportional to the square root of the diffusion time. Because the basis is symmetric under the inter-

change of u and q , the same formalism can be applied to data obtained by varying the diffusion time while keeping the diffusion gradient strength fixed.

The analyses we have presented have focused entirely on one-dimensional data and provides details of the 1D-SHORE framework introduced for the first time in Ref. [26]. Although we presented results from reconstructions of two- and three-dimensional propagators, these results were based on axially-symmetric or isotropic geometries, respectively. In these geometries, having the q -space data along one direction is tantamount to having it on the entire plane or within the entire three-dimensional space making it possible to compute the higher-dimensional propagators using one-dimensional transforms (see Eqs. 33 and 49). However, because of the separation of variables of the higher-dimensional analog of the simple harmonic oscillator Hamiltonian in Eq. 11, our scheme has a trivial extension to two- and three-dimensional q -space signals even in the absence of axial symmetry or isotropy as we showed in [28]. A similar approach was introduced in Ref. [1] that uses Gauss-Laguerre functions. We envision that representing the MR signal attenuation analytically in a series of orthogonal functions will have many applications. Most recently, the 1D-SHORE framework was shown to be useful in accurately estimating the moments of the underlying compartment size distributions, which could be employed to obtain new forms of MR image contrast [30].

5 Conclusion

We have introduced a new basis to represent one-dimensional q -space signal and reconstruct the average propagators from it. The basis is well-known in quantum mechanics, but some characteristics of the basis make it particularly relevant to and useful for q -space MR. Among these is its capability to accommodate complex-valued signals while ensuring a real and normalized average propagator. Additionally, the Fourier transform of each component is readily available making it possible to reconstruct the average propagators immediately. Similarly, useful descriptors of the propagator such as return-to-origin probabilities and its moments can be computed from the basis representation. On several simulations, the accuracy of the estimations was assessed and we demonstrated that it successfully represents signal profiles even when the signal and the propagators have unusual forms such as in the presence of diffraction-like features. Unlike the previously employed cumulant expansion, multi-exponential fitting and similar approaches, the basis functions are complete, orthogonal and the estimation/reconstruction scheme is linear with a wider range of applicability.

Acknowledgments

This research was supported by the Intramural Research Program of the Eunice Kennedy Shriver National Institute of Child Health and Human Development (NICHD) at the National Institutes of Health (NIH) and the Department of Defense in the Center for Neuroscience and Regenerative Medicine (CNRM).

Appendix 1. Remarks on the basis functions

Note that the functions $\psi_n(u, x)$, defined in Eq. 9 are the solutions to the eigenvalue equation

$$\left(-u^2 \frac{\partial^2}{\partial x^2} + \frac{x^2}{u^2}\right) \psi_n(u, x) = \lambda_n \psi_n(u, x), \quad (11)$$

with eigenvalues $\lambda_n = (2n + 1)$. Taking the Fourier transform of both sides, it is easy to show that the functions $\phi_n(u, q)$ are the solutions to the eigenvalue equation

$$\left(-\frac{1}{(2\pi u)^2} \frac{\partial^2}{\partial q^2} + (2\pi u)^2 q^2\right) \phi_n(u, q) = \lambda_n \phi_n(u, q). \quad (12)$$

Since Eqs. 11 and 12 are identical upon the transformations $x \rightarrow q$ and $u \rightarrow (2\pi u)^{-1}$, ψ_n and ϕ_n have the same form up to a multiplicative factor (see Eq. 9). In fact, the operator on the left hand side of these eigenvalue equations is the Hamiltonian operator with a quadratic potential, which describes the simple harmonic oscillator problem in quantum mechanics. However, our definitions of the eigenfunctions are slightly different from their forms as commonly used in quantum mechanics. Specifically, our basis is not normalized, but the scaling is such that when diffusion is Gaussian, $a_n = \delta_{n0}$, where δ_{ij} is the Kronecker delta.

Despite these minor differences from the basis used in quantum mechanics, our basis functions still satisfy the relationships

$$A \psi_n(u, z) = \begin{cases} 0 & , n = 0 \\ \sqrt{n} \psi_{n-1}(u, z) & , n \geq 1 \end{cases} \quad (13)$$

and

$$\tilde{A} \phi_n(u, q) = \begin{cases} 0 & , n = 0 \\ \sqrt{n} \phi_{n-1}(u, q) & , n \geq 1 \end{cases}, \quad (14)$$

where A and \tilde{A} are the “lowering operators” defined by

$$A = \frac{1}{\sqrt{2}} \left(\frac{z}{u} + u \frac{d}{dz} \right) \quad (15)$$

and

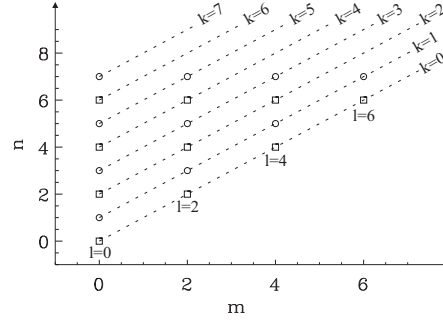


Fig. 8 Transformation of the indices n and m into k and l . Note that $N = 8$ in this figure.

$$\tilde{A} = \frac{i}{\sqrt{2}} \left(2\pi u q + \frac{1}{2\pi u} \frac{d}{dq} \right). \quad (16)$$

Writing the polynomials in the definitions of $E(q)$ and $P(x)$ in power series

It is possible to show that the Hermite polynomials can be written as [8]

$$H_n(x) = \sum_{m=0,2,4,\dots}^n (-1)^{m/2} \frac{2^{n-m} n!}{(n-m)! (m/2)!} x^{n-m}. \quad (17)$$

Inserting this expression into Eq. 5, the following power series expansion for the signal decay is obtained

$$E(q) = e^{-2\pi^2 q^2 u^2} \sum_{n=0}^{N-1} a_n \sum_{m=0,2,4,\dots}^n \frac{i^{-n-m} 2^{-m+n/2} \sqrt{n!}}{(n-m)! (m/2)!} (2\pi q u)^{n-m}. \quad (18)$$

The double summation in the above expression can be recast by using the transformations $k = n - m$ ($k = 0, 1, 2, \dots, N-1$) and $l = m$ ($l = 0, 2, \dots, N-k-1$) as shown in Fig. 8:

$$E(q) = e^{-2\pi^2 q^2 u^2} \sum_{k=0}^{N-1} b_{Nk}(u) q^k, \quad (19)$$

where

$$b_{Nk}(u) = \frac{i^{-k} (2\pi u)^k}{k!} \sum_{l=0,2,\dots}^{N-k-1} \frac{\sqrt{2^{k-l} (k+l)!}}{(l/2)!} a_{k+l}. \quad (20)$$

Using the same approach, the propagator can be written as

$$P(x) = e^{-x^2/(2u^2)} \sum_{k=0}^{N-1} c_{Nk}(u) x^k, \quad (21)$$

where

$$c_{Nk}(u) = \frac{1}{\sqrt{2\pi} u^{k+1} k!} \sum_{l=0,2,\dots}^{N-k-1} (-1)^{l/2} \frac{\sqrt{2^{k-l}} (k+l)!}{(l/2)!} a_{k+l}. \quad (22)$$

Moments of $P(x)$ and $P(0)$

The m -th order moment of $P(x)$ is defined to be

$$\langle x^m \rangle = \int_{-\infty}^{\infty} dx x^m P(x). \quad (23)$$

The usual strategy to compute the moments of a propagator from its $E(q)$ profile, involves the power series expansion of the plane wave in the Fourier relationship between the signal and the probability, i.e.,

$$\begin{aligned} E(q) &= \int_{-\infty}^{\infty} dx e^{-i2\pi qx} P(x) \\ &= 1 + \frac{(-i2\pi q)}{1!} \langle x \rangle + \frac{(-i2\pi q)^2}{2!} \langle x^2 \rangle + \frac{(-i2\pi q)^3}{3!} \langle x^3 \rangle + \dots \end{aligned} \quad (24)$$

Therefore, a power series representation of $E(q)$ data, upon a term-by-term comparison with Eq. 24 would yield the moments of $P(x)$.

However, the moments can be computed directly using the Hermite function representation of the $E(q)$ profile as well. This can be done by inserting Eqs. 21-22 into 23 yielding

$$\langle x^m \rangle = u^m \sum_{k=0,2,\dots}^{N-1} \frac{(k+m-1)!!}{k!} \sum_{l=0,2,\dots}^{N-k-1} (-1)^{l/2} \frac{\sqrt{2^{k-l}} (k+l)!}{(l/2)!} a_{k+l}, \quad (25)$$

when m is even. Odd ordered moments can be computed using essentially the same expression where the index k takes odd values, i.e., $k = 1, 3, 5, \dots$

Note that $P(0)$ can be evaluated conveniently by setting $x = 0$ in Eq. 21, i.e.,

$$P(0) = c_{N0}(u). \quad (26)$$

Note that $P(x=0)$ is not a true return-to-origin probability, but, since $P(x)$ is obtained through a one-dimensional Fourier transform, it is the probability for the molecules to return to the yz -plane—a consequence of the Fourier slice theorem.

Appendix 2. The rectangular pore

When the spins are trapped between two infinite plates, one located at $x = 0$ and the other at $x = L$, the expected signal intensity at long diffusion times is given by [40]

$$E^{\text{rect}}(q) = \frac{\sin^2(\pi qL)}{(\pi qL)^2}, \quad (27)$$

where it is implied that the diffusion gradients are applied perpendicular to the infinite plates. The corresponding average propagator is

$$P^{\text{rect}}(x) = \begin{cases} \frac{L-|x|}{L^2}, & |x| \leq L \\ 0, & |x| > L \end{cases}. \quad (28)$$

Obviously, the return-to- yz -plane probability is simply

$$P^{\text{rect}}(0) = \frac{1}{L}. \quad (29)$$

Finally, the even order moments of the propagator are given as

$$\langle x^m \rangle^{\text{rect}} = \frac{2L^m}{(m+1)(m+2)}, \quad (30)$$

while the odd order moments vanish.

Appendix 3. Axially symmetric geometries and the cylindrical pore

General results

Many geometries of interest have an anisotropic structure with an oblate or prolate shape, where the environment possesses a symmetry axis. In our treatment we shall take the z -axis to be along this symmetry axis. In such an axially symmetric or transversely isotropic process, the same signal attenuation profile is obtained when the diffusion gradient is applied in any direction (which defines the x -axis in our treatment) perpendicular to the symmetry axis. In this case, a two-dimensional isotropic Fourier transform can be evaluated from one-dimensional q -space data, i.e.,

$$P_{2D}(\mathbf{r}) = \int_{-\infty}^{\infty} dq_x \int_{-\infty}^{\infty} dq_y e^{i2\pi\mathbf{q}\cdot\mathbf{r}} E(q), \quad (31)$$

where the two-dimensional vectors \mathbf{q} and \mathbf{r} reside on the xy -plane. The radial and polar coordinates of these vectors shall be denoted to be (q, θ_q) and (r, θ_r) , respec-

tively. Inserting the Rayleigh expansion for two-dimensional plane waves,

$$e^{i2\pi\mathbf{q}\cdot\mathbf{r}} = \sum_{m=-\infty}^{\infty} i^m J_m(2\pi qr) e^{im(\theta_r - \theta_q)}, \quad (32)$$

into Eq. 31, the two-dimensional isotropic propagator for axially symmetric environments is obtained to be

$$P_{2D}(r) = 2\pi \int_0^{\infty} dq q J_0(2\pi qr) E(q). \quad (33)$$

The same analysis can be repeated for the inverse Fourier transform, yielding

$$E(q) = 2\pi \int_0^{\infty} dr r J_0(2\pi qr) P_{2D}(r). \quad (34)$$

The one-dimensional average propagator, obtained from a one-dimensional Fourier transform, is related to the two-dimensional propagator via the relation

$$\begin{aligned} P(x) &= \int_{-\infty}^{\infty} dy P_{2D}(x, y) \\ &= 2 \int_{|x|}^{\infty} P_{2D}(r) \frac{r}{\sqrt{r^2 - x^2}} dr, \end{aligned} \quad (35)$$

which is a consequence of the Fourier slice theorem. Clearly, the above expression is just the Abel transform [3] of $P_{2D}(r)$. Therefore, the inverse Abel transform of the one-dimensional projection reveals the two-dimensional axially symmetric propagator to be

$$P_{2D}(r) = -\frac{1}{\pi} \int_r^{\infty} \frac{P'(x)}{\sqrt{x^2 - r^2}} dx. \quad (36)$$

The return-to- yz -plane probability can be estimated from the two-dimensional axially symmetric propagator:

$$P(x=0) = 2 \int_0^{\infty} dr P_{2D}(r). \quad (37)$$

On the other hand, a return-to- z -axis probability can be calculated by setting $r=0$ in Eq. 33, i.e.,

$$P_{2D}(0) = 2\pi \int_0^{\infty} dq q E(q). \quad (38)$$

The radial moments of the two-dimensional axially symmetric propagator are defined as

$$\langle r^m \rangle_{2D} = 2\pi \int_0^{\infty} dr r^{m+1} P_{2D}(r). \quad (39)$$

Similar to what is done in Eq. 24, the Bessel function in Eq. 34 can be written as a power series, yielding

$$E(q) = 1 - \frac{(2\pi q)^2}{2^2} \langle r^2 \rangle_{2D} + \frac{(2\pi q)^4}{(2 \cdot 4)^2} \langle r^4 \rangle_{2D} - \frac{(2\pi q)^6}{(2 \cdot 4 \cdot 6)^2} \langle r^6 \rangle_{2D} + \dots \quad (40)$$

A term-by-term comparison of the series in Eqs. 24 and 40 suggests that the radial moments are given in terms of the one-dimensional moments by the relationship

$$\langle r^m \rangle_{2D} = \frac{m!!}{(m-1)!!} \langle x^m \rangle. \quad (41)$$

Note that this relationship holds only when m is even; axial symmetry implies that odd order moments of the one-dimensional propagator, $\langle x^m \rangle$, will vanish.

Estimates in terms of a_n coefficients

Inserting Eq. 19 into Eq. 33 yields [8]

$$P_{2D}(r) = \sum_{k=0}^{N-1} b_{Nk}(u) \frac{\Gamma(k/2+1)}{2^{k/2+1} \pi^{k+1} u^{k+2}} {}_1F_1\left(\frac{k}{2}+1, 1, -\frac{r^2}{2u^2}\right), \quad (42)$$

where ${}_1F_1(\alpha, \gamma; z)$ is the confluent hypergeometric function of the first kind. Standard computational libraries do not include an implementation of these functions. However, a simple and accurate implementation can be performed by exploiting the recurrence relation [8]

$$\alpha {}_1F_1(\alpha+1, \gamma; z) = (z+2\alpha-\gamma) {}_1F_1(\alpha, \gamma; z) + (\gamma-\alpha) {}_1F_1(\alpha-1, \gamma; z). \quad (43)$$

Since ${}_1F_1(\alpha, \gamma; 0) = 1$, a return-to- z -axis probability can be computed simply by summing up the factors before the confluent hypergeometric function in Eq. 42. Note that the radial moments, $\langle r^m \rangle_{2D}$ can be computed from a_n by using Eq. 25 along with Eq. 41.

The cylindrical pore

In this section we shall consider restricted diffusion within a cylinder of radius r_0 , which is an example to an axially symmetric process. The MR signal attenuation is given by [17]

$$E^{\text{cyl}}(q) = \left(\frac{J_1(2\pi q r_0)}{\pi q r_0} \right)^2. \quad (44)$$

By inserting Eq. 44 into 33, the two-dimensional axially symmetric propagator can be evaluated to be

$$P_{2D}^{\text{cyl}}(r) = \begin{cases} \frac{4 \cos^{-1}\left(\frac{r}{2r_0}\right) - \frac{r}{r_0} \sqrt{4 - \left(\frac{r}{r_0}\right)^2}}{2\pi^2 r_0^2}, & r \leq 2r_0 \\ 0, & r > 2r_0 \end{cases} . \quad (45)$$

It immediately follows that the return-to- z -axis probability is given by

$$P_{2D}^{\text{cyl}}(0) = \frac{1}{\pi r_0^2} . \quad (46)$$

Moreover, the return-to- yz -plane probability was calculated, by inserting Eq. 45 into Eq. 37, to be

$$P^{\text{cyl}}(x=0) = \frac{16}{3\pi^2 r_0} . \quad (47)$$

Finally, the radial moments are given by

$$\langle r^m \rangle_{2D}^{\text{cyl}} = \frac{2^{m+4} (m+1)!!}{(m+2)(m+4)!!} r_0^m . \quad (48)$$

Note that $\langle x^m \rangle$ can be calculated by inserting this expression into Eq. 41.

Appendix 4. Isotropic geometries and the spherical pore

General results

Many specimens of interest in pulsed-field-gradient MR are isotropic. Even in the presence of local anisotropy [29, 24, 22], the randomness in the shape and orientation of the pores would lead to isotropy due to the averaging of signals from individual compartments. In such environments, having the q -space data with diffusion gradients applied along a single direction is tantamount to having the data all across the three-dimensional q -space. Therefore, it is possible to characterize the entire average propagators and related parameters via one-dimensional sampling. In fact, the resulting three-dimensional isotropic propagator can be computed through the relationship

$$P_{3D}(R) = \frac{2}{R} \int_0^\infty dq q \sin(2\pi q R) E(q) , \quad (49)$$

which is obtained by inserting the Rayleigh expansion of three-dimensional plane-waves [31]

$$e^{i2\pi \mathbf{q} \cdot \mathbf{R}} = 4\pi \sum_{l=0}^{\infty} i^l j_l(2\pi q R) \sum_{m=-l}^l Y_{lm}(\mathbf{R}/R) Y_{lm}(\mathbf{q}/q)^* \quad (50)$$

into the 3D Fourier transform relationship between $E(\mathbf{q})$ and $P(\mathbf{R})$ in Eq. 1, where $q = |\mathbf{q}|$, $R = |\mathbf{R}|$ and \mathbf{q} and \mathbf{R} are three-dimensional vectors. The Fourier slice theo-

rem enables to establish the relation between the three-dimensional isotropic propagator and one-dimensional propagator:

$$\begin{aligned}
P(x) &= \int_{-\infty}^{\infty} dy \int_{-\infty}^{\infty} dz P_{3D}(\sqrt{x^2 + y^2 + z^2}) \\
&= 2\pi \int_0^{\infty} d\rho \rho P_{3D}(\sqrt{\rho^2 + x^2}) \\
&= 2\pi \int_{|x|}^{\infty} dR R P_{3D}(R) .
\end{aligned} \tag{51}$$

Here the first step involves the change of variables $\rho^2 = y^2 + z^2$. Similarly, the transformation $R^2 = x^2 + \rho^2$ was employed in the second step. Taking the derivative of both sides with respect to x and subsequently employing the fundamental theorem of calculus, one obtains

$$P_{3D}(R) = \left(-\frac{1}{2\pi x} \frac{dP(x)}{dx} \right) \Big|_{x=R} . \tag{52}$$

Eq. 51 implies that the return-to- yz -plane probability can be calculated using the relationship

$$P(x=0) = 2\pi \int_0^{\infty} dR R P_{3D}(R) . \tag{53}$$

Note that Eq. 49 leaves the return-to-origin probability undetermined, which should be calculated using the relationship

$$P_{3D}(0) = 4\pi \int_0^{\infty} dq q^2 E(q) . \tag{54}$$

The radial moments of the three-dimensional isotropic propagator are defined as

$$\langle R^m \rangle_{3D} = 4\pi \int_0^{\infty} dR R^{m+2} P_{3D}(R) . \tag{55}$$

Inserting Eq. 52 into the above expression and performing integration by parts, it is straightforward to show that the radial moments of the three-dimensional isotropic propagator and the moments of the one-dimensional propagator are related through the relationship

$$\langle R^m \rangle_{3D} = (m+1) \langle x^m \rangle . \tag{56}$$

Note that this relationship holds only when m is even. Odd order moments of the one-dimensional propagator, $\langle x^m \rangle$, vanish due to isotropy.

Estimates in terms of a_n coefficients

By inserting the expansion of the one-dimensional propagator in Eq. 8 into Eq. 52 and differentiating by using the relationships in Eqs. 13 and 15, one can expand the three-dimensional isotropic propagator as

$$P_{3D}(R) = \sum_{n=0}^{N-1} a_n \xi_n(u, R), \quad (57)$$

where

$$\xi_n(u, R) = \begin{cases} \frac{1}{2\pi u^2} \Psi_0(u, R) & , n = 0 \\ \frac{1}{2\pi u^2} \Psi_n(u, R) - \sqrt{\frac{n}{2}} \frac{1}{\pi u R} \Psi_{n-1}(u, R) & , n \geq 1 \end{cases}. \quad (58)$$

Note that the return-to-origin probability can be estimated from the coefficients a_n by setting $R = 0$ in the above expression. Finally, the radial moments, $\langle R^m \rangle_{3D}$ can be computed from a_n by using Eq. 25 along with Eq. 56.

The spherical pore

Diffusion inside a spherical pore of radius R_0 , yields the following MR signal attenuation at long diffusion times [40]:

$$E^{\text{sph}}(q) = \left[\frac{3}{(2\pi q R_0)^2} \left(\frac{\sin(2\pi q R_0)}{2\pi q R_0} - \cos(2\pi q R_0) \right) \right]^2. \quad (59)$$

By inserting Eq. 59 into 49, one can evaluate the three-dimensional isotropic propagator to be

$$P_{3D}^{\text{sph}}(R) = \begin{cases} \frac{3(2R_0 - R)^2(4R_0 + R)}{64\pi R_0^6} & , R \leq 2R_0 \\ 0 & , R > 2R_0 \end{cases}. \quad (60)$$

It immediately follows that the return-to-origin probability is given by

$$P_{3D}^{\text{sph}}(0) = \frac{3}{4\pi R_0^3}. \quad (61)$$

The one-dimensional propagator can be obtained via a one-dimensional Fourier transform of $E^{\text{sph}}(q)$ or by inserting Eq. 60 into Eq. 51. In either case, it is given by

$$P^{\text{sph}}(x) = \begin{cases} \frac{3(2R_0 - |x|)^3(4R_0^2 + 6R_0|x| + x^2)}{160R_0^6} & , |x| \leq 2R_0 \\ 0 & , |x| > 2R_0 \end{cases}, \quad (62)$$

which implies that the return-to- yz -plane probability is given by

$$P^{\text{sph}}(x=0) = \frac{3}{5R_0}. \quad (63)$$

Since isotropic geometries are also axially symmetric, the expressions derived in Appendix 3 apply also to this appendix. For brevity, we shall include only the result for the return to long axis probability predicted for spherical pores:

$$P_{2\text{D}}^{\text{sph}}(0) = \frac{9}{8\pi R_0^2}. \quad (64)$$

Finally, the radial moments are given by

$$\langle R^m \rangle_{3\text{D}}^{\text{sph}} = \frac{9 \cdot 2^{m+3}}{m^3 + 13m^2 + 54m + 72} R_0^m. \quad (65)$$

Note that $\langle x^m \rangle$ can be calculated using this expression along with Eq. 56.

References

1. Assemlal, H.E., Tschumperlé, D., Brun, L.: Efficient and robust computation of PDF features from diffusion MR signal. *Med Image Anal* **13**(5), 715–729 (2009). DOI 10.1016/j.media.2009.06.004. URL <http://dx.doi.org/10.1016/j.media.2009.06.004>
2. Bennett, K.M., Schmainda, K.M., Bennett(Tong), R., Rowe, D.B., Lu, H., Hyde, J.S.: Characterization of continuously distributed cortical water diffusion rates with a stretched-exponential model. *Magn Reson Med* **50**(4), 727–734 (2003)
3. Bracewell, R.N.: *The Fourier Transform and its Applications*. McGraw-Hill, New York (1978)
4. Callaghan, P.T., Coy, A., MacGowan, D., Packer, K.J., Zelaya, F.O.: Diffraction-like effects in NMR diffusion studies of fluids in porous solids. *Nature* **351**, 467–469 (1991)
5. Cohen, Y., Assaf, Y.: High b-value q-space analyzed diffusion-weighted MRS and MRI in neuronal tissues — a technical review. *NMR Biomed* **15**, 516–542 (2002)
6. Cory, D.G., Garroway, A.N.: Measurement of translational displacement probabilities by NMR: An indicator of compartmentation. *Magn Reson Med* **14**(3), 435–444 (1990)
7. Fröhlich, A.F., Østergaard, L., Kiselev, V.G.: Effect of impermeable boundaries on diffusion-attenuated MR signal. *J Magn Reson* **179**(2), 223–233 (2006). DOI 10.1016/j.jmr.2005.12.005. URL <http://dx.doi.org/10.1016/j.jmr.2005.12.005>
8. Gradshteyn, I.S., Ryzhik, I.M.: *Table of integrals, series and products*. Academic Press (2000)
9. Hahn, E.L.: Spin echoes. *Phys Rev* **80**, 580–594 (1950)
10. Hürlimann, M.D., Schwartz, L.M., Sen, P.N.: Probability of return to origin at short times: A probe of microstructure in porous media. *Phys Rev B* **51**(21), 14,936–14,940 (1995)
11. Jensen, J.H., Helpert, J.A., Ramani, A., Lu, H., Kaczynski, K.: Diffusional kurtosis imaging: the quantification of non-Gaussian water diffusion by means of magnetic resonance imaging. *Magn Reson Med* **53**, 1432–1440 (2005)
12. Jian, B., Vemuri, B.C., Özarslan, E., Carney, P.R., Mareci, T.H.: A novel tensor distribution model for the diffusion-weighted MR signal. *NeuroImage* **37**(1), 164–176 (2007). DOI 10.1016/j.neuroimage.2007.03.074. URL <http://dx.doi.org/10.1016/j.neuroimage.2007.03.074>
13. Kärgler, J., Heink, W.: The propagator representation of molecular transport in microporous crystallites. *J Magn Reson* **51**(1), 1–7 (1983)
14. Kiselev, V.G., Il'yasov, K.A.: Is the “biexponential diffusion” biexponential? *Magn Reson Med* **57**(3), 464–469 (2007). DOI 10.1002/mrm.21164. URL <http://dx.doi.org/10.1002/mrm.21164>

15. Köpf, M., Metzler, R., Haferkamp, O., Nonnenmacher, T.F.: NMR studies of anomalous diffusion in biological tissues: Experimental observation of Lévy stable processes. In: G.A. Losa, D. Merlini, T.F. Nonnenmacher, E.R. Weibel (eds.) *Fractals in Biology and Medicine*, vol. 2, pp. 354–364. Birkhäuser, Basel (1998)
16. Liu, C.L., Bammer, R., Moseley, M.E.: Generalized diffusion tensor imaging (GDTI): A method for characterizing and imaging diffusion anisotropy caused by non-Gaussian diffusion. *Isr J Chem* **43**(1–2), 145–154 (2003)
17. McCall, D.W., Douglass, D.C., Anderson, E.W.: Self-diffusion studies by means of nuclear magnetic resonance spin-echo techniques. *Ber Bunsenges Phys Chem* **67**, 336–340 (1963)
18. Mitra, P.P., Sen, P.N.: Effects of microgeometry and surface relaxation on NMR pulsed-field-gradient experiments: Simple pore geometries. *Phys Rev B* **45**, 143–156 (1992)
19. Mulkern, R.V., Gudbjartsson, H., Westin, C.F., Zengingönül, H.P., Gartner, W., Guttman, C.R., Robertson, R.L., Kyriakos, W., Schwartz, R., Holtzman, D., Jolesz, F.A., Maier, S.E.: Multi-component apparent diffusion coefficients in human brain. *NMR Biomed* **12**(1), 51–62 (1999)
20. Niendorf, T., Dijkhuizen, R.M., Norris, D.G., van Lookeren Campagne, M., Nicolay, K.: Bi-exponential diffusion attenuation in various states of brain tissue: implications for diffusion-weighted imaging. *Magn Reson Med* **36**(6), 847–857 (1996)
21. Ohanian, H.C.: *Principles of quantum mechanics*. Prentice-Hall (1990)
22. Özarlan, E.: Compartment shape anisotropy (CSA) revealed by double pulsed field gradient MR. *J Magn Reson* **199**(1), 56–67 (2009). DOI 10.1016/j.jmr.2009.04.002. URL <http://dx.doi.org/10.1016/j.jmr.2009.04.002>
23. Özarlan, E., Basser, P.J.: MR diffusion - “diffraction” phenomenon in multi-pulse-field-gradient experiments. *J Magn Reson* **188**(2), 285–294 (2007). DOI 10.1016/j.jmr.2007.08.002. URL <http://dx.doi.org/10.1016/j.jmr.2007.08.002>
24. Özarlan, E., Basser, P.J.: Microscopic anisotropy revealed by NMR double pulsed field gradient experiments with arbitrary timing parameters. *J Chem Phys* **128**(15), 154,511 (2008). DOI 10.1063/1.2905765. URL <http://dx.doi.org/10.1063/1.2905765>
25. Özarlan, E., Basser, P.J., Shepherd, T.M., Thelwall, P.E., Vemuri, B.C., Blackband, S.J.: Observation of anomalous diffusion in excised tissue by characterizing the diffusion-time dependence of the MR signal. *J Magn Reson* **183**(2), 315–323 (2006). DOI 10.1016/j.jmr.2006.08.009. URL <http://dx.doi.org/10.1016/j.jmr.2006.08.009>
26. Özarlan, E., Koay, C.G., Basser, P.J.: Simple harmonic oscillator based estimation and reconstruction for one-dimensional q -space MR. In: *Proc. Intl. Soc. Mag. Reson. Med.*, vol. 16, p. 35 (2008)
27. Özarlan, E., Koay, C.G., Basser, P.J.: Remarks on q -space MR propagator in partially restricted, axially-symmetric, and isotropic environments. *Magn Reson Imaging* **27**(6), 834–844 (2009). DOI 10.1016/j.mri.2009.01.005. URL <http://dx.doi.org/10.1016/j.mri.2009.01.005>
28. Özarlan, E., Koay, C.G., Shepherd, T.M., Blackband, S.J., Basser, P.J.: Simple harmonic oscillator based reconstruction and estimation for three-dimensional q -space MRI. In: *Proc. Intl. Soc. Mag. Reson. Med.*, vol. 17, p. 1396 (2009)
29. Özarlan, E., Nevo, U., Basser, P.J.: Anisotropy induced by macroscopic boundaries: Surface-normal mapping using diffusion-weighted imaging. *Biophys J* **94**(7), 2809–2818 (2008). DOI 10.1529/biophysj.107.124081. URL <http://dx.doi.org/10.1529/biophysj.107.124081>
30. Özarlan, E., Shemesh, N., Koay, C.G., Cohen, Y., Basser, P.J.: Nuclear magnetic resonance characterization of general compartment size distributions. *New J Phys* **13**, 015,010 (2011)
31. Özarlan, E., Shepherd, T.M., Vemuri, B.C., Blackband, S.J., Mareci, T.H.: Resolution of complex tissue microarchitecture using the diffusion orientation transform (DOT). *NeuroImage* **31**(3), 1086–1103 (2006). DOI 10.1016/j.neuroimage.2006.01.024. URL <http://dx.doi.org/10.1016/j.neuroimage.2006.01.024>
32. Pawula, R.F.: Approximation of the linear Boltzmann equation by the Fokker-Planck equation. *Phys Rev* **162**, 186–188 (1967)
33. Pfeuffer, J., Provencher, S.W., Gruetter, R.: Water diffusion in rat brain in vivo as detected at very large b values is multicompartmental. *MAGMA* **8**(2), 98–108 (1999)

34. Press, W.H., Teukolsky, S.A., Vetterling, W.T., Flannery, B.P.: Numerical Recipes in C: The Art of Scientific Computing. Cambridge Press, Cambridge (1992)
35. Schwartz, S.C.: Estimation of probability density by an orthogonal series. *Ann Math Statist* **38**, 1261–1265 (1967)
36. Silva, M.D., Helmer, K.G., Lee, J.H., Han, S.S., Springer, C.S., Sotak, C.H.: Deconvolution of compartmental water diffusion coefficients in yeast-cell suspensions using combined T_1 and diffusion measurements. *J Magn Reson* **156**(1), 52–63 (2002). DOI 10.1006/jmre.2002.2527. URL <http://dx.doi.org/10.1006/jmre.2002.2527>
37. Stejskal, E.O.: Use of spin echoes in a pulsed magnetic-field gradient to study anisotropic, restricted diffusion and flow. *J Chem Phys* **43**(10), 3597–3603 (1965)
38. Stejskal, E.O., Tanner, J.E.: Spin diffusion measurements: Spin echoes in the presence of a time-dependent field gradient. *J Chem Phys* **42**(1), 288–292 (1965)
39. Stepišnik, J.: Analysis of NMR self-diffusion measurements by a density matrix calculation. *Physica B & C* **104**, 350–364 (1981)
40. Tanner, J.E., Stejskal, E.O.: Restricted self-diffusion of protons in colloidal systems by the pulsed-gradient, spin-echo method. *J Chem Phys* **49**(4), 1768–1777 (1968)
41. Walter, G.G.: Properties of Hermite series estimation of probability density. *Ann Statist* **5**, 1258–1264 (1977)
42. Yablonskiy, D.A., Bretthorst, G.L., Ackerman, J.J.: Statistical model for diffusion attenuated MR signal. *Magn Reson Med* **50**(4), 664–669 (2003)